

High-Performance 3D Li-B-C-Al Alloy Anode and its Twofold Li Electrostripping and Plating Mechanism Revealed by Synchrotron X-Ray Tomography

Fengcheng Tang, Xia Zhang, Markus Osenberg, Chao Yang, Haifeng Huang, André Hilger, Masyuki Uesugi, Kentaro Uesug, Akihisa Takeuchi, Ingo Manke, Fu Sun* , and Libao Chen* 

The uncontrollable Li electrostripping and plating process that results in dendritic Li growth and huge volume change of Li anode limits the practicality of Li metal batteries (LMBs). To simultaneously address these issues, designing three-dimensional (3D), lithiophilic and mechanically robust electrodes seems to be one of the cost-effective strategies. Herein, a new 3D Li-B-C-Al alloy anode is designed and fabricated. The prepared 3D alloy anode exhibits not only superior lithiophilicity that facilitates uniform Li nucleation and growth but also sufficient mechanical stability that maintains its structural integrity. Superior performance of the prepared 3D alloy is demonstrated through comprehensive electrochemical tests. In addition, non-destructive and 3D synchrotron X-ray computed tomography (SX-CT) technique is employed to investigate the underlying working mechanisms of the prepared alloy anode. A unique twofold Li electrostripping and plating mechanism under different electrochemical cycling conditions is revealed. Lastly, improved performance of the full cells built with the 3D alloy anode and $\text{LiNi}_{0.8}\text{Co}_{0.1}\text{Mn}_{0.1}\text{O}_2$ (NCM811) cathode corroborate its potential application capability. Overall, the current work not only showcases the superiority of the 3D alloy as potential anode material for LMBs but also provides fundamental insights into its underlying working mechanisms that may further propel its research and development.

1. Introduction

It has been widely accepted that developing clean and sustainable energy technologies to replace the conventional fossil fuels becomes crucial and vital when it comes to decreasing the global greenhouse-gas concentration that hit record high in the past years.^[1] The rechargeable lithium-ion battery (LIB) technology, which can efficiently store and/or convert chemical energy to electrical energy, seems to be one of the auspicious solutions. Recently, it has been penetrating universally in our daily lives, e.g., the 3 C electronic devices, electric vehicles (EVs) and the fast-growing grid scale battery storage stationary plants. However, the state-of-the-art LIBs are suffering from meeting the booming global energy demand because they have almost reached their theoretical capacity limits.^[2] Lithium metal batteries (LMBs), which are built with Li metal anodes that possess the highest theoretical specific capacity (3860 mA h g^{-1}) and the lowest electrochemical potential (-3.04 V vs SHE), are regarded as one of the most promising next-generation battery technologies.^[3] Nevertheless, their practical application has been hindered heavily by the serious safety issues and unsatisfyingly low Coulombic efficiency (CE).^[4,5] The root cause is generally acknowledged as the uncontrollable growth of Li dendrites and the continuous accumulation of dead Li during repeated Li electrochemical deposition and dissolution.^[3]

To tackle the abovementioned challenges, tremendous efforts are devoted to achieve a controllable Li electrodeposition and dissolution by using electrolyte additives, artificial solid electrolyte interface (SEI) films, modified separators and novel structured electrodes.^[3] The employment of electrolyte additives or artificial SEI proved effective to prevent Li dendrites growth, yet they became less functional during ultra-long cycling due to the gradual depletion or decomposition of the key components.^[6] The modified separators could alleviate the safety issues to some extent, yet their synthesis procedures were usually cumbersome and almost of all them could inevitably increase the interfacial resistance.^[7] On the basis of the Sand's model, which mathematically describes the time of dendrite growth (τ_s) and the local current density (J^{-2}), it is suggested that constructing 3D porous electrode structures would be an effective approach to fundamentally suppress dendritic Li

To tackle the abovementioned challenges, tremendous efforts are devoted to achieve a controllable Li electrodeposition and dissolution by using electrolyte additives, artificial solid electrolyte interface (SEI) films, modified separators and novel structured electrodes.^[3] The employment of electrolyte additives or artificial SEI proved effective to prevent Li dendrites growth, yet they became less functional during ultra-long cycling due to the gradual depletion or decomposition of the key components.^[6] The modified separators could alleviate the safety issues to some extent, yet their synthesis procedures were usually cumbersome and almost of all them could inevitably increase the interfacial resistance.^[7] On the basis of the Sand's model, which mathematically describes the time of dendrite growth (τ_s) and the local current density (J^{-2}), it is suggested that constructing 3D porous electrode structures would be an effective approach to fundamentally suppress dendritic Li

F. C. Tang, Prof. L. B. Chen

State Key Laboratory of Powder Metallurgy, Central South University, Changsha 410083, China

E-mail: lbchen@csu.edu.cn

F. C. Tang Dr. F. Sun, X. Zhang

Qingdao Institute of Bioenergy and Bioprocess Technology, Chinese Academy of Sciences, Qingdao 266101, China

E-mail: sunfu@qibebt.ac.cn

M. Osenberg, C. Yang, Dr. A. Hilger, Dr. I. Manke

Helmholtz-Zentrum Berlin für Materialien und Energie, 14109 Berlin Germany

H. Huang

College of Chemistry and Chemical Engineering, Central South University, Changsha 410083, China

M. Uesugi, K. Uesug, A. Takeuchi

Japan Synchrotron Radiation Research Institute (JASRI)/ Spring-8, Sayo-gun Hyogo 679-5198, Japan

 The ORCID identification number(s) for the author(s) of this article can be found under <https://doi.org/10.1002/eem2.12387>.

DOI: 10.1002/eem2.12387

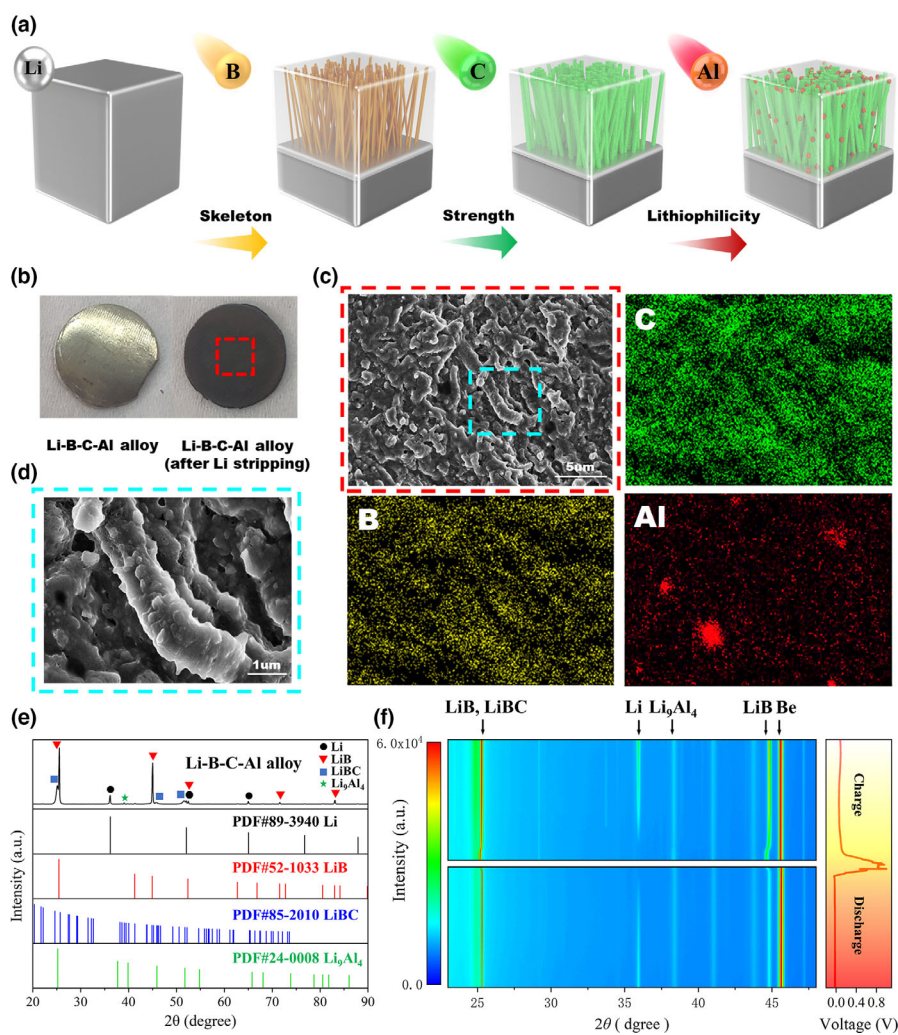


Figure 1. a) Schematic diagram of the design concept of the 3D Li-B-C-Al alloy. b) The digital images of the 3D Li-B-C-Al alloy before and after Li stripping. c) SEM and EDS mapping of the Li-B-C-Al alloy after Li stripping and the EDS mapping shows C, B and Al elements. d) SEM image showing the surface morphology of the skeleton fiber. e) XRD patterns of the 3D Li-B-C-Al alloy. f) Contour maps of the *in situ* XRD patterns collected during the first cycle of the Li₉Li-B-C-Al cell at 0.2 mA cm⁻².

growth due to their ultra-high specific surface area that could reduce the local current density.^[4] Moreover, the 3D structures could also act as a “host” for accommodating massive Li electrodeposits, thereby alleviating the volume change of Li anodes during long-lasting electrochemical cycling.^[8–10] Previous studies showed that the *ex situ* formed 3D skeletons, such as metal-based foams or carbon-based frameworks, could effectively suppress the Li dendrites formation and improve the battery CE.^[11–13] Unfortunately, these 3D architectures have difficulties in simultaneously controlling the Li nucleation sites and maintaining structural integrity due to their lithiophobic and mechanically soft skeletons. Hence tailoring their lithiophilicity chemistry and mechanical strength becomes crucial in developing structured 3D electrodes. Under this circumstance, several lithiophilic–lithiophobic hybrid and mechanically robust scaffolds were reported.^[14,15] Nevertheless, the manufacturing of these hybrid 3D scaffolds is time-consuming and costly,

which poses a series challenge for their broad and massive applications. From the material’s point of view, Li alloy stands out due to its superior lithiophilic property and mass production capability.^[16–18] Although several types of Li alloys have been previously prepared, yet an ideal 3D Li alloy electrode possessing simultaneously high specific surface area, intrinsic lithiophilicity, sufficient mechanical stability and cost-effective manufacturing procedure has to be designed.^[19]

Apart from that, clarifying the fundamental performance-improvement mechanisms of the 3D structured electrodes could provide valuable and enlightening insights guiding their further development. In this regard, several probing techniques, e.g., scanning electron microscopy (SEM) and atomic force microscopy (AFM) have been employed to characterize the Li electrodeposits morphology formed on the cycled 3D electrodes.^[2,20] Similarly, nuclear magnetic resonance (NMR) was used to study the Li electroplating process.^[21] Nevertheless, it is worth noting that these probing techniques are mostly *ex situ* and they struggle to provide reliable information of the cycled 3D electrodes. What’s more, these probing techniques usually yield 2D information that is hard to comprehensively illustrate the inherent 3D nature of the studied samples. For these reasons, *in situ* and 3D characterization methods that can non-destructively probe the electrochemically induced changes within the engineered 3D electrodes is urgently needed.^[22–25]

The above discussions highlight the importance of manufacturing an ideal 3D Li alloy anode in a cost-effective way as well as clarifying its fundamental working mechanisms. In this work, a new 3D Li-B-C-Al alloy electrode is successfully manufactured by the smelting and rolling procedure and its working mechanisms for accommodating Li under different electrochemical cycling conditions are clarified. The *in situ* formed compound fibers, which possess high Li⁺ ion diffusion coefficient, serve as interconnected 3D skeleton of the 3D alloy electrode. Moreover, the addition of Al and C elements could respectively regulate the Li nucleation sites and enhance the mechanical property of the 3D alloy electrode. Extensive electrochemical tests of the cells built with the 3D Li-B-C-Al alloy anode show an enhanced cyclability and rate capability. Additionally, non-destructive and 3D synchrotron X-ray computed tomography technique (SX-CT), together with the post-mortem SEM were employed to reveal the fundamental mechanisms for the improved electrochemical performance. These characterization results unravel a unique twofold Li-storage mechanism. In the last,

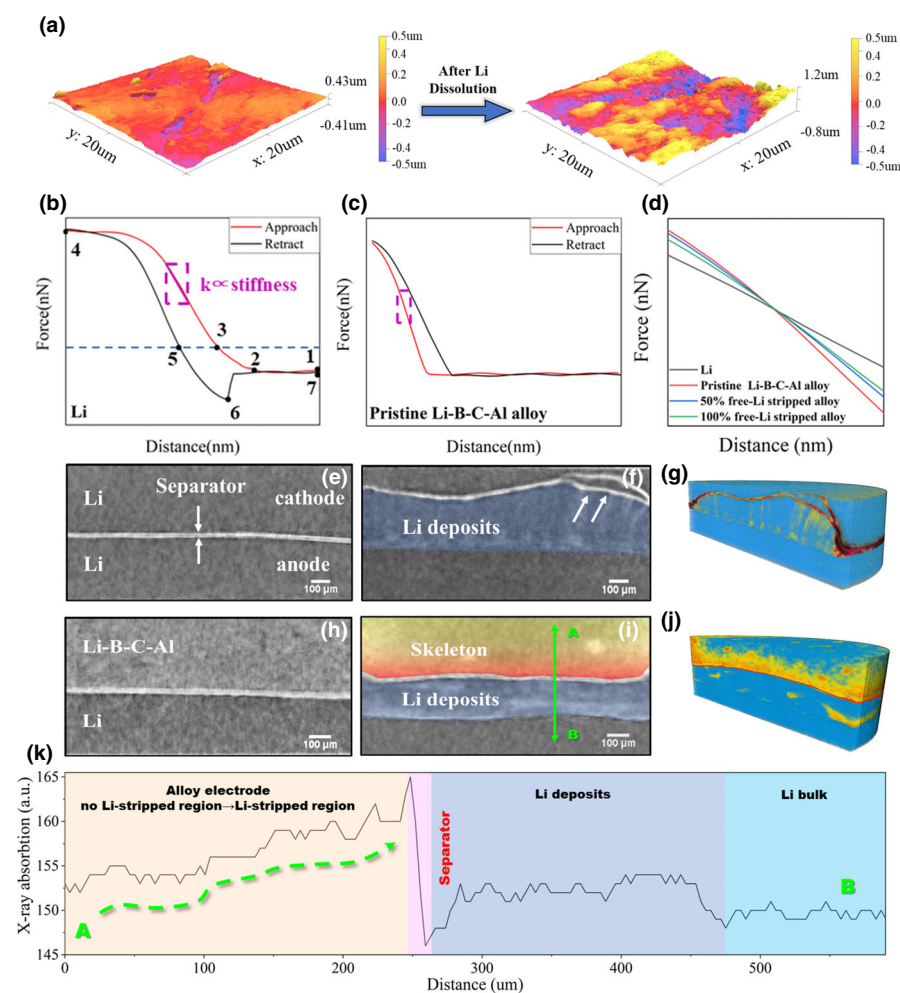


Figure 2. a) AFM images of the pristine (left) and 50% free-Li stripped Li-B-C-Al alloy (right). b, c) The force-distance curve recorded during the AFM measurement of Li foil b) and pristine Li-B-C-Al alloy c). d) Comparison of the slopes of the four curves in the purple dash box in b, c) and Figure S8(a,b). e, f) Reconstructed X-ray tomography slice of the pristine Li symmetric cell e) and the charged Li symmetric cell f). h, i) Reconstructed X-ray tomography slice of the pristine Li_{0.8}Li-B-C-Al cell h) and the charged Li_{0.8}Li-B-C-Al cell i). g, j) show the corresponding 3D renderings of f), i). k) X-ray absorption changes along the green double-headed arrow line in i).

performance measurement results demonstrate notable high-rate capability and long-term cyclability of the full cells built with the 3D Li-B-C-Al alloy anode and high voltage LiNi_{0.8}Co_{0.1}Mn_{0.1}O₂ (NCM811) cathode. Overall, the current work not only showcases the superiority of the reported 3D alloy as anode material for LMBs but also provides fundamental insights into its working mechanisms that enable its outstanding electrochemical performance.

2. Results and Discussion

2.1. Morphology, Composition, and Structure Characterization of the 3D Li-B-C-Al Anode

Figure 1a schematically illustrates the design concept of the 3D Li-B-C-Al alloy. Firstly, introducing B into Li matrix could in situ form

the Li-B compound skeleton, which has high Li⁺ ion diffusion coefficient and superior electronic conductivity.^[26] Secondly, the C doping significantly enhances the mechanical strength of the scaffold skeleton, forming the mechanically robust 3D alloy framework.^[27] Finally, the added Al serves as homogeneously distributed lithiophilic Li nucleation sites due to its excellent lithiophilicity.^[28] The detailed manufacturing procedure of the 3D Li-B-C-Al alloy is depicted in Figure S1 and the corresponding mass ratio (wt%) is listed in Table S1.^[2] In the 3D Li-B-C-Al alloy anode, only the free-Li (not bonded in Li-B compound) will be used during electrochemical cycling. And the theoretical specific capacity is calculated to be 1582 mA h/g, as shown in Figure S2a. To experimentally confirm this, Li electrodedissolution from the 3D alloy anode in a Li_{0.8}Li-B-C-Al cell was conducted and the result is shown in Figure S2b. This experiment shows that 1575.3 mA h g⁻¹ can be obtained by using the free-Li within the 3D alloy anode (corresponding to the dissolved Li below 0.1 V), in agreement with the theoretical calculation. Figure S2b also shows that the subsequent dissolution of Li > 0.1 V can be attributed to the decomposition of the Li-B compound.^[2]

The morphology and the composition of the 3D alloy electrode were further characterized. Figure 1b exhibits that it has a yellowish metallic color before Li electrostripping and it changes into dark afterwards (the corresponding electrochemical curve is shown in Figure S2). Figure 1c shows the corresponding SEM result of the stripped 3D alloy electrode (corresponding to the red dash rectangle in Figure 1b), from which one can distinguishably note the interconnected skeleton fibers that form the 3D scaffold of the alloy electrode. Besides, the EDS mappings in Figure 1c demonstrate that the constituting B and C elements are distributed uniformly throughout the fibers while the Al phase tends to coalesce. The zoomed-in view of the skeleton fiber (blue dash rectangle in Figure 1c) is shown in Figure 1d. These characterizations demonstrate that the prepared 3D Li-B-C-Al alloy is consisted of free-Li, 3D skeleton Li-B(C) phase and Al phase.

To analyze its compositional structure, X-ray diffraction (XRD) was employed (Figure 1e). One can note two noticeable peaks located at 25.5° and 45° assigned to LiB phase (PDF#52–1033) and one weak peak located at 36° for metallic Li (PDF#89–3940), corroborating the coexistence of skeleton Li-B and free-Li. The remaining peaks correspond well to the Li₉Al₄ phase (PDF#24–0008) and LiBC phase (PDF#85–2010). The existence of Li₉Al₄ intermetallic compound is foreseeable according to the binary phase diagram (Figure S3a) and

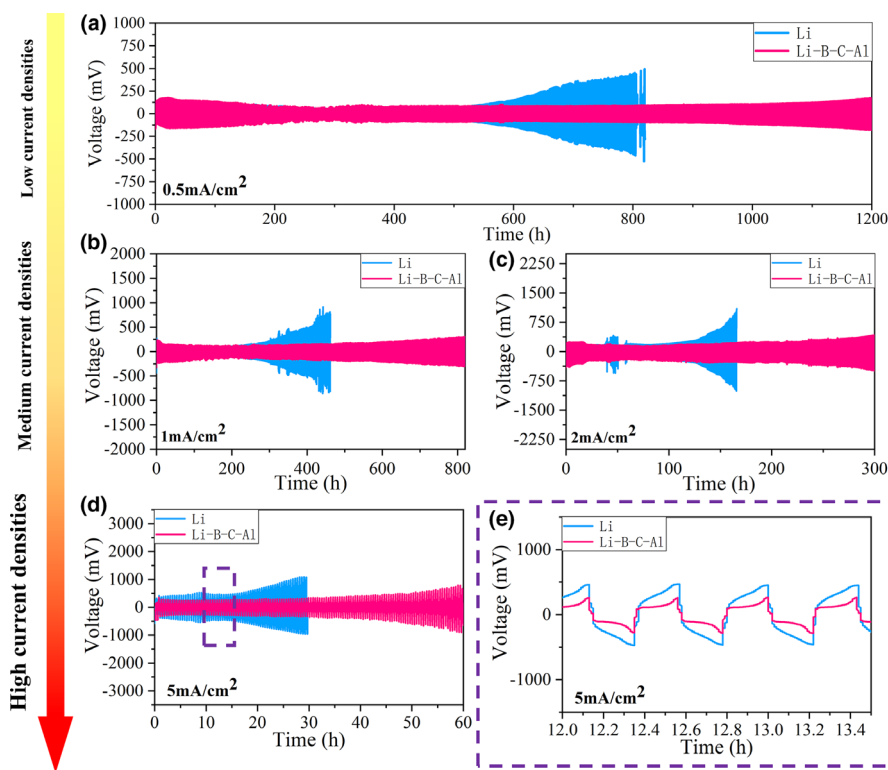


Figure 3. Comparison of the galvanostatic cyclability of the Li symmetric cell and Li-B-C-Al symmetric cell using carbonate electrolyte at a) 0.5 mA cm^{-2} , b) 1 mA cm^{-2} , c) 2 mA cm^{-2} at 0.5 mAh cm^{-2} area capacity. d) The galvanostatic cycling curve of the cells at 5 mA cm^{-2} at 1 mAh cm^{-2} area capacity. e) The enlarged view shown in the purple dash rectangle in d).

Figure S3b shows that the Li_9Al_4 phase can lower the Li nucleation energy barrier during Li electroplating due to its lithiophilicity.^[16,29] In addition, the hexagonal crystal LiBC phase plays a key role in enhancing the mechanical property of the 3D alloy electrode and regulating the Li^+ ion flux during Li electroplating due to its high elasticity modulus and Li^+ ionic conductivity, as shown in Figure S4–S5 and Table S2.^[30] The above analysis suggests that the robust skeleton fibers and numerous lithiophilic sites of the 3D Li-B-C-Al alloy could facilitate Li electrostripping and plating, which is further studied by the in situ XRD measurement.

The in situ XRD characterization results of the Li electrostripping/plating from/to the 3D Li-B-C-Al alloy anode are shown in Figure 1f. From this figure, one can obviously note that the XRD peak at 36° , which corresponds to the free-Li, gradually fades during the charge (stripping) and reappears steadily in the following discharge (plating). This result suggests that it is the free-Li that contributes to the specific capacity of the 3D alloy anode. In addition, it is noticeable that the LiB phase peaks at 25.5° and 45° shift to a lower degree when the voltage is higher than 0.1 V and this phenomenon disappears during the following Li plating process, suggesting that the LiB compound undergoes reversible transformation during delithiation/lithiation process.^[31] Furthermore, no change occurs to the LiBC and Li_9Al_4 peaks, implying that they do not participate in the Li electrostripping/plating process. These results indicate that the 3D Li-B-C-Al alloy can efficiently provide

reversible capacity while maintain its structure integrity upon cycling.

2.2. Mechanical Property and Structural Integrity of the 3D Li-B-C-Al Anode

The mechanical property and the structural integrity of the prepared 3D Li-B-C-Al alloy anode were studied by AFM and laboratory X-ray computed tomography (CT) techniques. Figure 2a shows that the smooth surface of the 3D alloy anode became uneven after Li electrostripping, indicating that some of the LiB and LiBC skeleton fibers are exposed after 50% free-Li was removed. This is confirmed by the SEM cross-sections shown in Figure S6. To reveal the effect of these skeleton fibers on the mechanical properties of the 3D alloy anode, AFM measurement using the contact mode was performed on the 100% free-Li stripped Li-B-C-Al alloy, 50% free-Li stripped Li-B-C-Al alloy, pristine Li-B-C-Al alloy, and pure Li. The detailed illustration of the AFM measurement is shown in Figure S7, during which process the measured tip force and the tip displacement distance are recorded simultaneously.^[32] It is the slope of this force-distance curve measured during the loading step (from step 3 to step 4 in Figure S7) that can be used to qualitatively describe the elastic strength of the measured sample. The measured force-distance curves of these four samples are shown in Figure 2b,c and Figure S8. The linear fit of the slopes of these four force-distance curves (marked as k) is shown in Figure 2d. A closer inspection of Figure 2d shows that the order of the mechanical strength of these four samples is: pristine 3D Li-B-C-Al alloy > 50% free-Li stripped alloy > 100% free-Li stripped alloy > Li. The higher mechanical strength of the pristine 3D alloy than the stripped ones (50% and 100% free-Li stripped) is resulted from the fiber strengthening effect,^[33] while the higher mechanical strength of the stripped alloys than that of Li is attributed to the high elasticity modulus of the LiB and LiBC (see Table S2).

In situ laboratory CT technique, which can provide straightforward visualization of the studied sample, was employed to study the structural integrity of the 3D Li-B-C-Al alloy anode. To this end, the Li symmetric cell and Li-B-C-Al|Li cell were comparatively studied after they were intentionally charged for 100 h (electrochemical curve is shown in Figure S9), mimicking the Li-stripping from Li and the 3D alloy anode (the cell design will be explained in the following section). The obtained internal morphologies are shown in Figure 2e–j. Figure 2e,h show respectively the cross-sections of the uncharged Li symmetric cell and Li-B-C-Al|Li cell, from which one can discernibly note the smooth and even electrode/seperator interface. Figure 2f shows that large quantities of Li electrodeposits are accumulated on the Li anode surface (blue color shadow) after $\sim 100 \text{ h}$ charging, forming bumpy mountain-like structure that ruptures the separator (white arrows). The formation of the bumpy structure may be caused by an

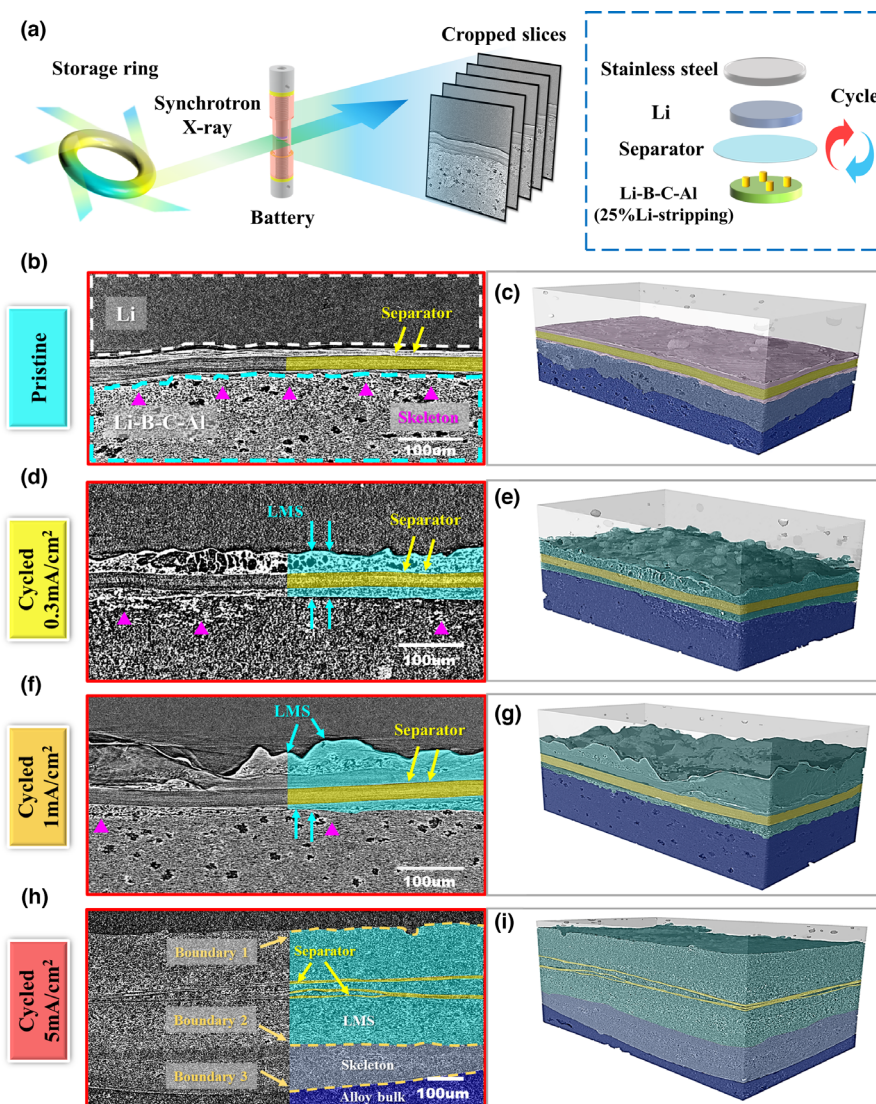


Figure 4. a) A schematic illustration of the synchrotron X-ray tomography technique and the battery components inside the tomography cell. b, c) Reconstructed X-ray tomography slice and the 3D rendering of the pristine $\text{Li}|\text{Li-B-C-Al}$ cell. Reconstructed X-ray tomography slice and the 3D rendering of the $\text{Li}|\text{Li-B-C-Al}$ cell after cycling at d, e) 0.3 mA cm^{-2} , f, g) 1 mA cm^{-2} and h, i) 5 mA cm^{-2} . All the scale bars are $100 \mu\text{m}$ long.

unregulated Li^+ ion flux during Li electroplating.^[23,34] In comparison, Figure 2i,j obviously show that flat and homogeneous Li electrodeposits are accumulated on Li anode without damaging the separator. The homogenous Li electrodeposition may be benefited from the well-distributed Li^+ ion flux dissolved from the robust 3D framework. In order to further study the phase change in the Li-stripped Li-B-C-Al skeleton region (Figure 2i, yellow-to-red gradient color shadow), X-ray absorption changes along the green double-head arrow line ($600 \mu\text{m}$ long, from A to B) was analyzed and the results are shown in Figure 2k. This figure shows that the X-ray absorption increases gradually from point A (no Li-stripped region) to the electrode/separator interface (Li-stripped region), indicating a stepwise Li stripping in the alloy anode. These CT results demonstrate superior structural integrity of the prepared 3D Li-B-C-Al alloy anode.

2.3. Electrochemical Performance of the 3D Li-B-C-Al Anode and the *In Situ* Synchrotron X-Ray Tomography Results

Electrochemical performance of the symmetric cells built with either the 3D alloy anode or Li metal were evaluated under different current densities ($0.5, 1$ and 2 mA cm^{-2}) at the same capacity (0.5 mAh cm^{-2}) and the results are shown in Figure 3a–c. Figure 3a shows that the symmetric cell assembled with the 3D Li-B-C-Al alloy can cycle stably for over 1200 cycles with low voltage hysteresis ($\sim 80.3 \text{ mV}$) at 0.5 mA cm^{-2} , while the Li symmetric cell experiences a rapid voltage polarization increase ($\sim 161.8 \text{ mV}$) after $<600 \text{ h}$ cycling. The improved cyclability of the Li-B-C-Al symmetric cells are also notable at 1 and 2 mA cm^{-2} , as shown respectively in Figure 3b,c. To further study its performance at higher current densities,^[35] the symmetric cells built with the 3D alloy anode were further studied under high current density condition (5 mA cm^{-2} at 1 mAh cm^{-2}) and high area capacity condition (1 mA cm^{-2} at 5 mAh cm^{-2} , Figure S10). Figure 3d,e show that the Li-B-C-Al symmetric cell also displays better cyclability than that of Li symmetric cell under this condition. Besides the carbonate-based electrolyte, enhanced cyclability of the 3D alloy anode was also corroborated in ether-based electrolyte and 5 V carbonate-based electrolytes (Figure S11). Moreover, Figure S12 shows that the symmetric cell built with the 3D alloy anode outperforms that built with the 3D Li-B alloy anode. To sum up, these

results suggest that the prepared 3D Li-B-C-Al anode possesses superior electrochemical performance than that of pure Li anode.

To fundamentally reveal the mechanistic reasons for the superior electrochemical performance of the 3D alloy anode, synchrotron X-ray CT (SX-CT) technique was employed to get an in-depth understanding of its Li electrostripping and plating mechanisms. Figure 4a and Figure S13 illustrate the specially designed tomography cell and the employed imaging beamline.^[34,36–38] For the SX-CT measurement, four different Li-B-C-Al|Li cells subjected to different cycling conditions were studied without battery disassembly and the results are shown in Figure 4 (the corresponding electrochemical curves are shown in Figure S14). Note that 25% free-Li of the Li-B-C-Al electrode utilized in the SX-CT characterizations was pre-stripped. More details can be found in the Experimental section.

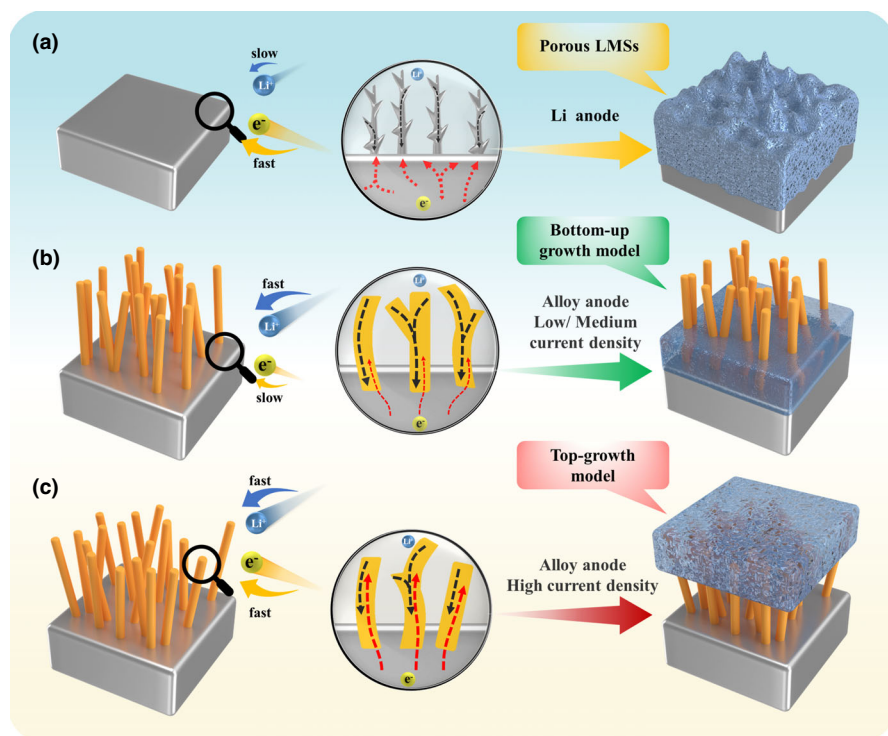


Figure 5. a) Schematic illustration of the Li electrostripping and plating on pure Li electrode. Schematics illustrating the twofold Li electrostripping and plating mechanism of the 3D Li-B-C-Al anode under b) low to medium current densities and c) high current density.

Figure 4b,c show respectively the cross-section and the 3D rendering of the uncycled Li⁺/Li-B-C-Al cell, from which one can clearly distinguish the Li metal electrode (white dash rectangle), Li-B-C-Al alloy (blue dash rectangle), free-Li stripped skeleton (the purple triangles correspond to the exposed skeleton) and the separator (yellow color shadow). For the cell galvanostatically cycled at 0.3 mA cm⁻² for 80 cycles (Figure S14a), Figure 4d,e show that an enormous amount of porous and rough Li electrodeposits are generated on the Li electrode side (blue color shadow, above the separator in Figure 4d). These porous lithium micro structures (LMSs) are mostly electrochemically inert and they accumulate on the Li electrode surface after repeated Li electrostripping and plating. This finding is in good agreement with our previous works.^[37,39,40] In contrast, negligible LMSs are noted on the Li-B-C-Al side (blue color shadow, below the separator in Figure 4d). Furthermore, Figure 4f,g illustrate that both the quantity and the extent of the inhomogeneity of the generated LMSs on the Li electrode side increase after the current density was increased to 1 mA cm⁻² at 1 mAh cm⁻² for 100 cycles (Figure S14b), evidencing the significant volume change of the pure Li metal due to its hostless nature (blue color shadow, above the separator in Figure 4f). In stark contrast, few LMSs accumulate on the Li-B-C-Al electrode side (blue color shadow, below the separator in Figure 4f) and the structural integrity of the Li-B-C-Al electrode is preserved, indicating that Li electroplating and stripping occurred mostly within the internal 3D skeleton. When the current density was further increased to 5 mA cm⁻² for 180 cycles (Figure S14c), Figure 4h,i unambiguously exhibit that significant amount of LMSs are generated on the Li electrode side (blue color

shadow, above the separator in Figure 4h) and the separator is delaminated into 3 layers (yellow color shadow in Figure 4h). The delamination of the Celgard 2325 separator into 3 separate layers is caused by the significant force generated during the irreversible transformation of bulk Li to porous LMSs.^[41] Moreover, on the Li-B-C-Al electrode side, one can clearly distinguish three stratified layers from its surface to its bulk (divided by orange dash lines boundary 2 and 3). These three layers are respectively the porous LMSs layer, the 3D skeleton layer (contains a small amount of Li) and the un-reacted bulk alloy (see more below).

The cross-sectional SX-CT results unambiguously demonstrate that the improved cyclability of the 3D Li-B-C-Al alloy electrode during low to medium current density cycling is attributed to its superior 3D structural integrity and the controlled Li electroplating/stripping. The SX-CT results clearly demonstrate that the mechanically robust scaffold fibers (AFM results in Figure 2) prevent the collapsing of the 3D alloy electrode during electrochemical cycling. In addition, the homogeneously distributed lithiophilic Li₉Al₄ phase (EDS mapping shown in Figure 1c) provides the preferential Li nucleation sites during Li electroplating. Moreover, a faster Li⁺ ion diffusion capability of the 3D Li-B-C-Al alloy anode, as indicated by the EIS analysis shown in Figure S15, facilitates a fast Li⁺ ion transportation into the inner region of the alloy anode during Li electroplating. These advantageous merits collaboratively migrate the incoming Li⁺ ion flux into the 3D electrode and homogenize the subsequent Li⁺ ion reduction, resulting in a bottom-up plating behavior. Taking the stepwise Li electrostripping behavior of the alloy electrode (shown in Figure 2) into consideration, these results indicate that the large volume variation during Li electrochemical cycling can be effectively accommodated by the 3D alloy anode, as vividly verified by the SX-CT results in Figure 4d-g.

On the other hand, the SX-CT results shown in Figure 4h,i reveal a different Li stripping and plating mechanism of the 3D Li-B-C-Al alloy electrode during high current density cycling. Figure 4h unambiguously shows three stratified layers from its surface to its bulk (divided by orange dash lines boundary 2 and 3), i.e., the top-most porous LMS layer, the 3D skeleton layer (contains a small amount of Li) and the bottom un-reacted bulk alloy. This phenomenon suggests that Li plating preferentially occurs on the top of the 3D alloy anode during high current density cycling instead of the locations during the low to medium current density cycling (Figure 4i vs Figure 4e,g). It is conjectured that under high current density condition, a higher extent of electric field would be generated within the 3D alloy anode during Li plating. And this intensified electric field could act as the main driving force in accelerating electrons migrating

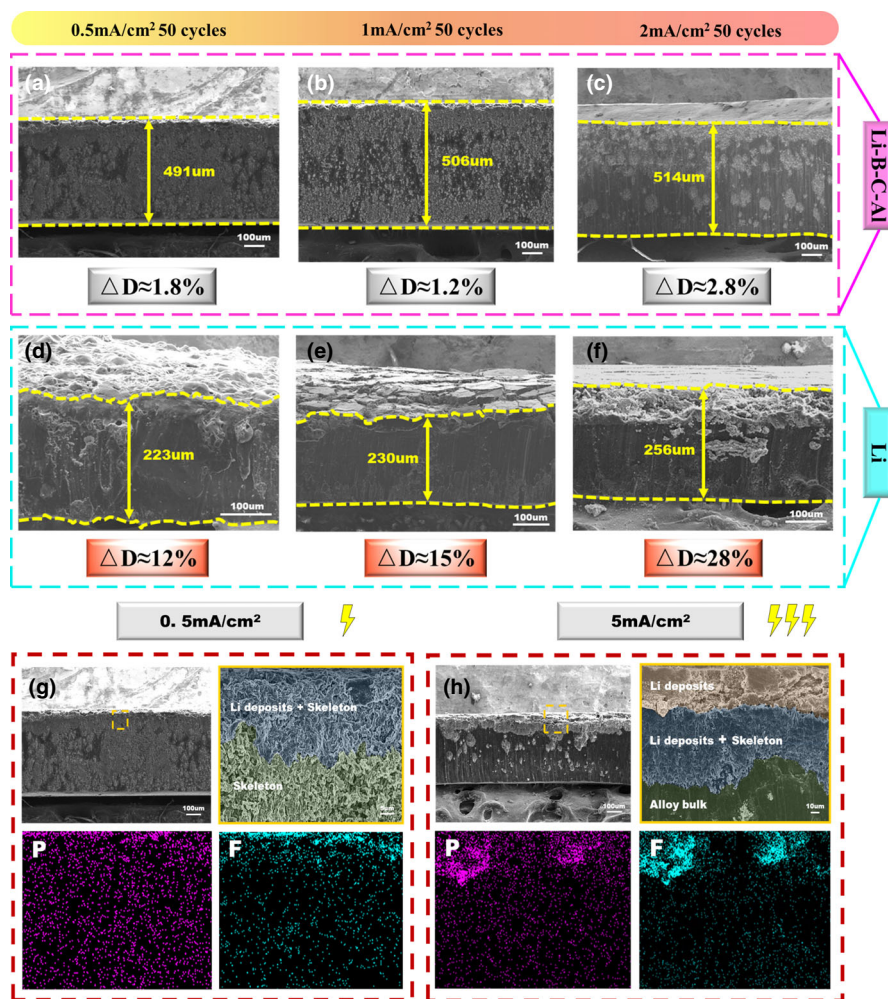


Figure 6. The SEM cross-sections of a) Li-B-C-Al electrode and d) Li electrode after 50 cycles at 0.5 mA cm^{-2} for 0.5 mAh cm^{-2} . SEM images of b) Li-B-C-Al and e) Li electrode after 50 cycles at 1 mA cm^{-2} . SEM images of c) Li-B-C-Al and f) Li electrode after 50 cycles at 2 mA cm^{-2} . The SEM cross-sections and EDS mapping of F and P element of Li-B-C-Al alloy after 50 cycles h) at 0.5 mA cm^{-2} with a capacity of 0.5 mAh cm^{-2} and h) at 5 mA cm^{-2} with a capacity of 1 mAh cm^{-2} .

upwards, resulting in the combination of ions and electrons at the top part of the 3D alloy electrode. Nevertheless, it is worth noting that the boundary between the LMS layer and the electrode skeleton layer is indistinct compared with the sharp boundary between the LMS layer and the Li electrode (boundary 2 vs boundary 1 in Figure 4h). This phenomenon indicates that at least some of the Li plating could also occur within the exposed 3D skeleton layer. The reason may be the ion-conductive and lithiophilic skeleton that facilitates the Li^+ ion transportation and Li nucleation. The generation of the 3D skeleton layer is caused by the continuous Li electrostripping from the 3D alloy electrode with partial Li electroplating therein. To conclude, the non-destructive synchrotron X-ray tomography characterization results provide straightforward and trustworthy evidence that the 3D Li-B-C-Al electrode possesses a unique twofold Li electrostripping and plating mechanism in mitigating the accumulation of uncontrollable LMSs.

2.4. The Twofold Li Electrostripping and Plating Mechanism and the Post-Mortem Characterization

Aiming to elucidate the unique twofold Li electrostripping and plating model of the 3D Li-B-C-Al alloy anode at different current densities, a schematic illustration derived from the abovementioned results is depicted in Figure 5. Figure 5a shows that a porous LMS layer is generated after Li cycling, which consists of uneven Li electrodeposits and electrochemically inert “dead Li.”^[42] Extended cycling of the Li anode results in the gradual and irreversible transformation of the original bulk Li to the accumulated LMSs, which is accompanied by an increase in inner cell resistance and concomitant cell degradation. In comparison, Figure 5b shows that Li electrodeposits are formed homogeneously within the 3D alloy anode and they grow in a bottom-up behavior under low to medium current densities. This bottom-up deposition behavior is caused by the ion-conductive and lithiophilic 3D skeleton that facilitate the migration of the incoming Li^+ ion flux into the interior of the 3D electrode, where they are then reduced. During Li stripping process, these well-regulated Li electrodeposits undergo stepwise dissolution because they are densely packed within an electronic and ionic conductive 3D skeleton (Figure 2i). Hence, few LMS agglomerates form on the top of the alloy anode during long-term cycling (Figure 4d,f). In addition, the 3D Li-B-C-Al electrode maintains its structural integrity during Li stripping due to its robust skeleton framework, in contrast to the collapse of pure Li anode. On the other hand, Figure 5c shows that a top-growth

model of Li electrodeposition occurs on the top surface of the 3D Li-B-C-Al alloy anode under high current densities. The reason for this growth on the top of the skeleton framework may be that the externally applied high current density may induce a strong local electric field, which in turn accelerates the transportation of electrons in the 3D alloy skeleton so that it exceeds that of Li^+ ion transportation. This scenario would lead to the preferential reduction of the incoming Li^+ ion flux on the upper part of the 3D anode and would result in the formation of a layer of LMSs (Figure 4h). Nevertheless, some of the Li plating could still occur within the exposed 3D skeleton layer due to its lithiophilic skeleton. Moreover, the Li electrodeposits formed on the top part of the 3D Li-B-C-Al alloy still exhibit a dense and homogeneous microstructure due to the large specific surface area and lithiophilic nature of the skeletons, compared to the Li electrodeposits formed on the Li electrode side. As a result, a lower voltage polarization and an extended lifespan of the alloy based symmetric cells are obtained (Figure 3d,e). To conclude, the 3D Li-B-C-Al alloy anode effectively

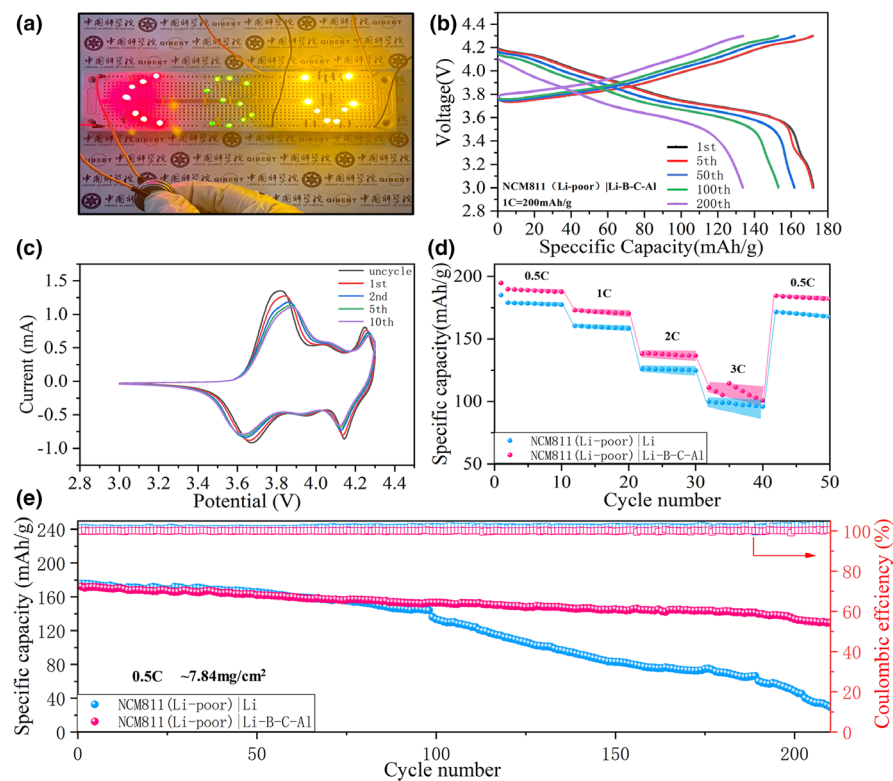


Figure 7. a) The figure showing that NCM811|Li-B-C-Al coin cells light up the LED lights. b) Charge–discharge profiles of the 1st, 5th, 50th and 200th cycle of the NCM811(Li-poor)|Li-B-C-Al coin cell (cathode mass loading of 7.84 mg cm^{-2}) at 0.5C. c) CV curves of the NCM811(Li-poor)|Li-B-C-Al coin cell at the 1st, 2nd, 5th and 10th cycle. d) Rate performance of the NCM811(Li-poor)|Li-B-C-Al coin cell at different current densities. e) Long-term cycling tests of NCM811(Li-poor)|Li-B-C-Al and NCM811(Li-poor)|Li coin cells at 0.5 C.

regulates and controls the LMSs via a unique twofold Li electrostripping and plating scheme during electrochemical cycling.

To experimentally confirm the unique twofold Li electrostripping and plating mechanism of the 3D Li-B-C-Al alloy anode revealed by non-destructive SX-CT technique, *ex situ* SEM characterizations of the cycled Li-B-C-Al and Li electrodes were studied and the results are shown in **Figure 6**. The SEM cross-sections in **Figure 6a–c** show that the cycled Li-B-C-Al electrodes (pristine 500 μm thick in **Figure S16a**) display negligible volume change (no more than $\sim 3\%$) after cycling under low to medium current densities (electrochemical curves shown in **Figure 3a–c**), in stark comparison to that of pure Li shown in **Figure 6d–f** (volume change $>12\%$, the pristine 200 μm thick Li is shown in **Figure S16b**). The structure stability of the 3D Li-B-C-Al alloy electrode is resulted from the homogeneous and controllable Li electrostripping/plating. The preferential location of the Li electrodeposition during low current density, i.e., the interior region of the 3D alloy anode, is also experimentally confirmed by the SEM results shown in **Figure S17**. In addition, **Figure 6g** shows that under 0.5 mA cm^{-2} , the 3D alloy anode can sufficiently accommodate the Li electrostripping and plating rather than forming Li dendrites, which is confirmed by the EDS mapping of P and F elements (P, F elements represent the SEI covering the Li deposits). **Figure S18** also reveals a relatively smooth and flat surface of the cycled 3D alloy anode. In contrast, dendritic or mossy Li electrodeposits are clearly

observable on the cycled Li surface. On the other hand, **Figure 6h** shows that at 5 mA cm^{-2} , the Li electrodeposits seem to accumulate on the surface part of the 3D alloy anode, as confirmed by the corresponding P and F EDS mapping. This finding suggests that the incoming Li^+ ion flux is preferentially reduced at the top part of the 3D alloy anode under high current density. Nevertheless, **Figure S19** shows that the Li electrodeposits formed on the surface of the cycled Li-B-C-Al electrode are denser and more homogeneous than that formed on the cycled Li foil. This is resulted from its high specific surface area and lithiophilicity nature. These experimental results provide complementary evidence for the unique two-fold Li electrostripping and plating mechanism of the 3D Li-B-C-Al alloy anode as well as its different Li-storage behavior compared with pure Li.

2.5. Performance Evaluation of the Full Cells Built with the 3D Li-B-C-Al Alloy

To evaluate the performance of the full cells built with the 3D alloy anode, it was paired with the $\text{LiNi}_{0.8}\text{Co}_{0.1}\text{Mn}_{0.1}\text{O}_2$ (NCM811) cathode materials and further measurements were conducted. As shown in **Figure 7a**, the NCM811|Li-B-C-Al coin cell with a cathode mass loading of $\sim 4.12 \text{ mg cm}^{-2}$ possesses sufficient working voltage to light up the LEDs. **Figure S20a–c** display the selected charge/discharge profiles of the built full cells cycled at 0.5 C ($1\text{C} = 200 \text{ mAh g}^{-1}$). **Figure S20d** compares the long-term cycling performance of the coin cells built with either 3D alloy anode or pure Li metal anode. One can note from **Figure S20d** that the NCM811|Li-B-C-Al coin cell delivers a stable capacity of $\sim 150.7 \text{ mAh g}^{-1}$ after 250 cycles at 0.5 C, corresponding to $\sim 81.3\%$ capacity retention. On the contrary, the capacity of the NCM811|Li coin cell decays from $\sim 183 \text{ mAh g}^{-1}$ to $\sim 120.5 \text{ mAh g}^{-1}$, corresponding to 65.8% capacity retention. **Figure S20e** further compares the rate performance of the coin cells built with different anodes, from which one can note that the NCM811|Li-B-C-Al coin cell possesses a better rate performance. These results demonstrate that long-lifespan and high-rate batteries could be obtained by using the 3D Li-B-C-Al alloy anode.

To further investigate the performance of the 3D Li-B-C-Al alloy anode under high cathode mass loading condition, it was paired with pre-delithiated $\sim 7.84 \text{ mg cm}^{-2}$ NCM811 cathode (named as NCM811 (Li-poor)) and the built cells were studied. It is expected that a reliable evaluation of the cyclability of the 3D alloy anode could be obtained by using the pre-delithiated cathode because all the cyclable Li^+ ions come from the alloy anode. The measurement results, with Li being the control sample, are shown in **Figure 7b–e**. **Figure 7b** shows that the NCM811(Li-poor)|Li-B-C-Al coin cell delivers a similar curve to the NCM811|Li-B-C-Al coin cell. **Figure 7c** shows the first 10 CV curves of

the NCM811(Li-poor)|Li-B-C-Al coin cell, displaying typical oxidation and reduction peaks of NCM811 cathode. Figure 7e shows that the NCM811(Li-poor)|Li-B-C-Al coin cell reaches a capacity retention of 75.6% after 200 cycles, which is similar to the above results (Figure S20). Figure 7d also shows that the NCM811(Li-poor)|Li-B-C-Al coin cell possesses a good rate performance. In contrast, the NCM811(Li-poor)|Li cell decays rapidly during both rate performance and long-term cycling tests (Figure 7d,e). These results demonstrate that the 3D Li-B-C-Al alloy anode possesses excellent electrochemical reversibility and superior rate capability, corroborating its feasibility and potential for practical applications.

3. Conclusion

In summary, a new 3D Li-B-C-Al alloy anode possessing improved electrochemical cycling performance was manufactured and its working mechanisms were studied by both in situ SX-CT characterization and post-mortem SEM measurements. The addition of Al, C elements brings superior mechanical property, excellent lithiophilicity and fast Li⁺ transportation capability to the in situ formed 3D Li-B skeleton fibers. These properties were confirmed by AFM, EIS and laboratory X-ray tomography techniques. Comprehensive electrochemical tests were conducted to evaluate the electrochemical performance of the 3D alloy anode and improved cycling performance in carbonate-based electrolyte, ether-based electrolyte and 5 V carbonate-based electrolyte were demonstrated. Non-destructive SX-CT technique revealed the unique twofold Li electrostripping and plating mechanism under different current densities of the 3D alloy anode, which was further corroborated by post-mortem SEM characterizations. In the last, practical application of the 3D alloy anode was evaluated by testing the NCM811|Li-B-C-Al full cells and the results show improved cyclability than the NCM811|Li full cells. In conclusion, our work not only demonstrates the fabrication of the high-performance 3D Li-B-C-Al alloy anode, but also unveils its fundamental working mechanisms during electrochemical cycling. It is expected that the current work would open new opportunities in designing novel 3D alloy anodes for next-generation LMBs.

4. Experimental Section

The Materials Preparation and Characterization, Battery preparation and electrochemical measurements, The tomography measurement are elaborately detailed in the Supporting Information.

Acknowledgements

Part of the SX-CT measurements were carried out at the BAMline instrument at the BESSY II electron storage ring operated by the Helmholtz-Zentrum Berlin für Materialien und Energie. Part of the SX-CT measurements were conducted at the BL20XU beamline at Spring-8 operated by the Japan Synchrotron Radiation Research Institute (JASRI). The project number is 2020A1079 at BL20XU. The work is supported by the National Natural Science Foundation of China (U1904216).

Conflict of Interest

The authors declare no conflict of interest.

Supporting Information

Supporting Information is available from the Wiley Online Library or from the author.

Keywords

Li alloy, Li metal anode, Li metal battery, Li-B-C-Al, plating

Received: January 27, 2022

Revised: March 7, 2022

Published online: March 19, 2022

- [1] A. Alyakhni, L. Boulon, J.-M. Vinassa, O. Briat, *IEEE Access* **2021**, 9, 143922.
- [2] C. Wu, H. Huang, W. Lu, Z. Wei, X. Ni, F. Sun, P. Qing, Z. Liu, J. Ma, W. Wei, *Adv. Sci.* **2020**, 7, 1902643.
- [3] D. Lin, Y. Liu, Y. Cui, *Nat. Nanotechnol.* **2017**, 12, 194.
- [4] X.-B. Cheng, R. Zhang, C.-Z. Zhao, Q. Zhang, *Chem. Rev.* **2017**, 117, 10403.
- [5] F. Sun, D. Zhou, X. Wang, I. Manke, L. Chen, *J. Energy Chem.* **2021**, 56, 34.
- [6] J. Deng, Y. Wang, S. Qu, Y. Liu, W. Zou, F. Zhou, A. Zhou, J. Li, *Batteries Supercaps* **2021**, 4, 140.
- [7] H. Zhuang, P. Zhao, G. Li, Y. Xu, X. Jia, *J. Power Sources* **2020**, 455, 227977.
- [8] S. Park, H. J. Jin, Y. S. Yun, *Adv. Mater.* **2020**, 32, 2002193.
- [9] H. Liu, M. Osenberg, L. Ni, A. Hilger, L. Chen, D. Zhou, K. Dong, T. Arlt, X. Yao, X. Wang, *J. Energy Chem.* **2021**, 61, 61.
- [10] T. Liu, J. Wang, Y. Xu, Y. Zhang, Y. Wang, *Nano-Micro Lett.* **2021**, DOI: <https://doi.org/10.1007/s40820-021-00687-3>.
- [11] J. Li, P. Zou, S. W. Chiang, W. Yao, Y. Wang, P. Liu, C. Liang, F. Kang, C. Yang, *Energy Storage Mater.* **2020**, 24, 700.
- [12] C.-P. Yang, Y.-X. Yin, S.-F. Zhang, N.-W. Li, Y.-G. Guo, *Nat. Commun.* **2015**, 6, 1.
- [13] B. Hong, H. Fan, X.-B. Cheng, X. Yan, S. Hong, Q. Dong, C. Gao, Z. Zhang, Y. Lai, Q. Zhang, *Energy Storage Mater.* **2019**, 16, 259.
- [14] H. Zhang, X. Liao, Y. Guan, Y. Xiang, M. Li, W. Zhang, X. Zhu, H. Ming, L. Lu, J. Qiu, *Nat. Commun.* **2018**, DOI: <https://doi.org/10.1038/s41467-018-06126-z>.
- [15] H. Shen, F. Qi, H. Li, P. Tang, X. Gao, S. Yang, Z. Hu, Z. Li, J. Tan, S. Bai, *Adv. Funct. Mater.* **2021**, 31, 2103309.
- [16] X. Gu, J. Dong, C. Lai, *Eng. Rep.* **2021**, 3, e12339.
- [17] W. Jia, Y. Liu, Z. Wang, F. Qing, J. Li, Y. Wang, R. Xiao, A. Zhou, G. Li, X. Yu, *Sci. Bull.* **1907**, 2020, 65.
- [18] H. Ye, Z. J. Zheng, H. R. Yao, S. C. Liu, T. T. Zuo, X. W. Wu, Y. X. Yin, N. W. Li, J. J. Gu, F. F. Cao, *Angew. Chem.* **2019**, 131, 1106.
- [19] S. Ni, S. Tan, Q. An, L. Mai, *J. Energy Chem.* **2020**, 44, 73.
- [20] X. Zhang, W. Wang, A. Wang, Y. Huang, K. Yuan, Z. Yu, J. Qiu, Y. Yang, *J. Mater. Chem. A* **2014**, 2, 11660.
- [21] Q. Liu, G. Zhu, R. Li, S. Lou, H. Huo, Y. Ma, J. An, C. Cao, F. Kong, Z. Jiang, *Energy Storage Mater.* **2021**, DOI: <https://doi.org/10.1016/j.jensm.2021.05.036>.
- [22] F. Tang, Z. Wu, C. Yang, M. Osenberg, A. Hilger, K. Dong, H. Markötter, I. Manke, F. Sun, L. Chen, *Small Methods* **2021**, 5, 2100557.
- [23] F. Sun, X. He, X. Jiang, M. Osenberg, J. Li, D. Zhou, K. Dong, A. Hilger, X. Zhu, R. Gao, *Mater. Today* **2019**, 27, 21.
- [24] Z. Yu, X. Zhang, C. Fu, H. Wang, M. Chen, G. Yin, H. Huo, J. Wang, *Adv. Energy Mater.* **2021**, 11, 2003250.
- [25] Z. Yu, J. Wang, L. Wang, Y. Xie, S. Lou, Z. Jiang, Y. Ren, S. Lee, P. Zuo, H. Huo, *ACS Energy Lett.* **2007**, 2019, 4.
- [26] X. B. Cheng, H. J. Peng, J. Q. Huang, F. Wei, Q. Zhang, *Small* **2014**, 10, 4257.

- [27] H. Huang, C. Wu, Z. Liu, X. Zeng, L. Chen, *Front. Chem.* **2020**, *8*, 781.
- [28] T. Zhang, H. Lu, J. Yang, Z. Xu, J. Wang, S.-I. Hirano, Y. Guo, C. Liang, *ACS Nano* **2020**, *14*, 5618.
- [29] H. Zhong, Y. Wu, F. Ding, L. Sang, Y. Mai, *Electrochim. Acta* **2019**, *304*, 255.
- [30] Q. Xu, C. Ban, A. C. Dillon, S.-H. Wei, Y. Zhao, *J. Phys. Chem. Lett.* **2011**, *2*, 1129.
- [31] Z. Liu, B. Huang, Z. Li, *Acta Metall. Sin-Engl.* **2004**, *17*, 667.
- [32] R. Hiesgen, S. Helmly, I. Galm, T. Morawietz, M. Handl, K. A. Friedrich, *Membranes* **2012**, *2*, 783.
- [33] L. Qi, S. Li, T. Zhang, J. Zhou, H. Li, *Compos. Struct.* **2019**, *209*, 328.
- [34] F. Sun, R. Moroni, K. Dong, H. Markötter, D. Zhou, A. Hilger, L. Zielke, R. Zengerle, S. Thiele, J. Banhart, *ACS Energy Lett.* **2017**, *2*, 94.
- [35] S. Jiao, J. Zheng, Q. Li, X. Li, M. H. Engelhard, R. Cao, J.-G. Zhang, W. Xu, *Joule* **2018**, *2*, 110.
- [36] F. Sun, L. Duchêne, M. Osenberg, S. Risse, C. Yang, L. Chen, N. Chen, Y. Huang, A. Hilger, K. Dong, *Nano Energy* **2021**, *82*, 105762.
- [37] F. Sun, D. Zhou, X. He, M. Osenberg, K. Dong, L. Chen, S. Mei, A. Hilger, H. Markötter, Y. Lu, *ACS Energy Lett.* **2019**, *5*, 152.
- [38] L. Ni, M. Osenberg, H. Liu, A. Hilger, L. Chen, D. Zhou, K. Dong, T. Arlt, X. Yao, X. Wang, *Nano Energy* **2021**, *83*, 105841.
- [39] F. Sun, L. Zielke, H. Markötter, A. Hilger, D. Zhou, R. Moroni, R. Zengerle, S. Thiele, J. Banhart, I. Manke, *ACS Nano* **2016**, *10*, 7990.
- [40] F. Sun, R. Gao, D. Zhou, M. Osenberg, K. Dong, N. Kardjilov, A. Hilger, H. Markötter, P. M. Bieker, X. Liu, *ACS Energy Lett.* **2018**, *4*, 306.
- [41] O. O. Taiwo, D. P. Finegan, J. Paz-Garcia, D. S. Eastwood, A. Bodey, C. Rau, S. Hall, D. J. Brett, P. D. Lee, P. R. Shearing, *Phys. Chem. Chem. Phys.* **2017**, *19*, 22111.
- [42] S. Wang, L. Zhang, X. Cai, T. Chu, D. Liu, C. Han, X. Qin, F. Kang, B. Li, *J. Mater. Chem. A* **2021**, *9*, 25004.